SIMULATION OF CRACK GROWTH IN ADHESIVELY BONDED JOINTS VIA COHESIVE ZONE MODELS

Nicola Zavatta[1], Maria Pia Falaschetti[1], Johan Birnie Hernández[1] and Enrico Troiani[1]

[1] University of Bologna, nicola.zavatta2@unibo.it

Abstract: Adhesively bonded joints have shown great advantages in the aerospace industry when compared with traditional mechanical fastening methods. These types of joints allow to reduce the overall structural weight, improve the fatigue life characteristics due to reduction of stress concentrations (uniform stress distribution), smooth external finish, sealed surfaces, and many others.
However, one of the main concerns with these joints is their characterization under fatigue loading, i.e., a comprehensive study of crack growth which will allow the development of standardized tests and certification in the aerospace sector. At the moment, their certification for primary structures requires that critical disbond be prevented by proper design. To this end, Disbond Arrest Features (DAFs) have been tested as a mean to improve the fatigue resistance of bonded joints.
In this work, the authors developed a numerical model to assess fatigue disbonding under mixed-mode loading, a condition which is frequently encountered in adhesive joints. The model was based on a cohesive zone formulation, which was implemented via user-defined subroutines UMAT in the finite element software Abaqus. Mixed mode disbonding was modelled through the Bürger's modification of Paris' law.
Two test cases were simulated: a double cantilever beam (DCB) specimen and a modified cracked-lap shear specimen with a bolted DAF. The results of the simulations were compared with experimental data from previous tests, showing that the model is able to reproduce the observed fatigue disbonding and capture the disbond arrest provided by the DAF.

Keywords: disbonding, crack growth, fatigue, FEM, cohesive zone model

INTRODUCTION

Aerospace engineers are constantly seeking out for lightweight materials with high strength and stiffness. Composite materials are extremely attractive since they offer high stiffness-to-weight and strength-to-weight ratios. The growing use of this type of materials has resulted in a great research effort for their development and certification. Not only their mechanical properties make them attractive for the aerospace sector, but also for the possibility of having single-part structures or embedding sensors into the matrix to monitor its state [1].
In modern commercial aircraft, the use of composite materials has become dominant, as seen in the Boeing 787 Dreamliner or the Airbus A350, were more of 50% weight of their structures is made of composite materials. The joints repairs in composite structures are mostly made with adhesives instead of mechanical fastening, and they are known as adhesively bonded joints [2]. These joints are characterized by the use of an epoxy adhesive, with high shear strength, to bond together two parts.

When compared to traditional mechanical fastening, i.e. bolts/rivets, adhesive bonds allow a uniform stress distribution over the joined surfaces and the reduction of stress concentrations since no holes are needed.
On the other hand, adhesive bonding presents two main issues: no reliable inspection technology for the quantification of the bond strength is available, and prediction models for crack growth under fatigue loading are still under development [3]. The latter is the focus of the present paper with the development of numerical models implemented in a commercial software for finite element simulations. User-defined subroutines have been developed in Abaqus finite element analysis commercial software via Cohesive Zone Models for the study of delamination growth in adhesively bonded joints under quasi-static and fatigue loading. The main advantage of this model is its flexibility, which allows it to be applied to mode I, mode II and mixed-mode loading conditions.
The development took as a reference the work by Zavatta [4, 5] on the study of delamination growth in adhesively bonded joints under quasi-static and fatigue loading.

THEORETICAL BACKGROUND

Delamination/Disbonding

Delamination refers to one of the most common failure modes in laminate fibre reinforced materials. The failure consists in the separation between two plies due to the difference between high interlaminar stresses and low through-thickness strength in the matrix [6]. It is a common point of failure since the fibres do not provide reinforcement through the thickness, and thus the load is carried by the matrix, which is known to be a brittle material.
In fracture mechanics, interlaminar fractures may be described by the three basic crack opening modes or a combination of these. The most common is the mode I, which is characterized by the opening of the crack due to tensile stresses normal to the crack plane. The double cantilever beam (DCB) specimen is used for the mode I testing.
The mode II is characterized by crack growth due to in-plane shear stresses (sliding between surfaces). The characterization of this mode is an on-going discussion, since there is no standardized specimen for this test, while the most popular is the End Notched Flexure (ENF). One of the main disadvantages of this specimen for mode II testing is the unstable crack propagation and the difficulty in measuring the crack length [7].
In most practical applications, a combination of mode I and II can be found. The cracked-lap shear (CLS) test specimen is of special interest for aeronautical structures, since it reproduces a shear-dominant mixed-mode ratio similar to the one seen in these structures (i.e. stringer-to-skin attachment). This specimen also gives an almost constant mix-mode ratio for different crack lengths [8], thus facilitating the study of crack-stopping design features.
In order to perform disbonding simulations, several modelling approaches have been developed over the years. One of the most effective is the Cohesive Zone Modelling (CZM), which will be discussed in the following section.

Crack Propagation by Cohesive Zone Modelling

Cohesive models [9] assume that fracture takes place in a region between two fictitious surfaces, called cohesive zone (Figure 1). The cohesive zone model enables progressive deterioration of the material, allowing for decreasing stress transfer as cracking occurs, according to a damage parameter D. The decrease of the traction strength is related to the separation of two virtual surfaces in the cohesive region and failure occurs when the traction strength becomes zero (D=1). The traction-separation constitutive law, which relates the traction strength to the separation in a nonlinear way, is shown in Figure 1 b) [10]. The parameters needed to define a bi-linear traction-separation law are: the maximum traction or cohesive strength t_{max}, which is related to material's strength, the separation at which maximum traction is reached (characteristic length δ_0) and the separation δ_c at which failure occurs, related to an admissible maximum displacement or to the fracture energy.

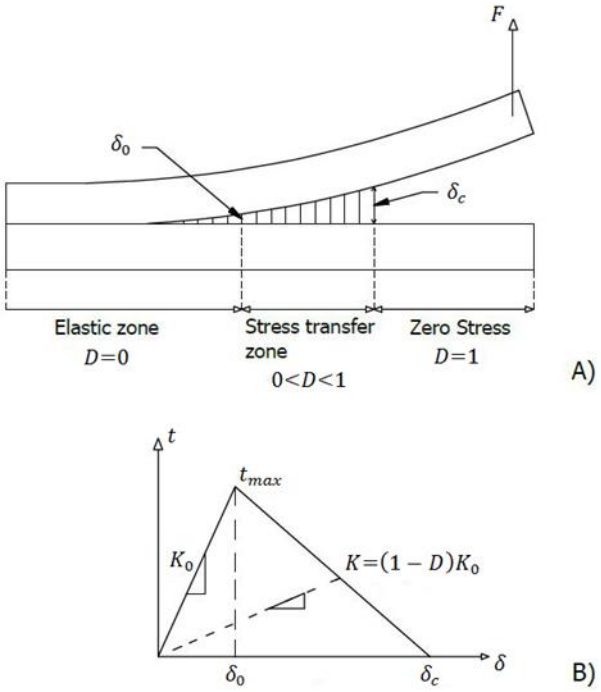

Figure 1 a) Scheme of the cohesive zone region. b) Traction-separation law.

The tractions (t_j) and displacements (δ_i) are related by a piecewise linear function t_j = t (δ_i). Furthermore, the rate of change can be defined as: $\dot{t}_j = D_{ji}^{tan}\dot{\delta}_i$.
The resulting constitutive equation is expressed as:

$$t_i = (1 - D)\delta_{ij}K\delta_j - D\delta_{ij}K\delta_{3j}\langle -\delta_3 \rangle \quad (1)$$

where D is the damage parameter, δ_{ij} is the Kronecker delta, K is the material's stiffness, $\langle\cdot\rangle$ the MacAuley bracket, defined as $\langle x \rangle = 1/2(x + |x|)$, and δ_3 is the (tensile) displacement in the normal direction.

In the quasi-static case, damage is expressed by:

$$D = \frac{\delta_c(\lambda - \delta_0)}{\lambda(\delta_c - \delta_0)} \quad (2)$$

Where $\lambda = \sqrt{{\delta_1}^2 + {\delta_2}^2 + \langle\delta_3\rangle^2}$ is the equivalent displacement jump.
To implement the cohesive zone model into a finite element simulation, some considerations should be made to ensure convergence. Specifically, the definition of the stiffness of the cohesive layer and the length of the cohesive zone are important to avoid a fictitious compliance before crack propagation and have enough elements to get an accurate result.
Turon [11] proposed that the stiffness of the cohesive zone be computed as:

$$K = \frac{\alpha E_3}{t} \quad (3)$$

where α is a parameter much larger than 1, that allows to capture the correct stiffness (α > 50), E_3 is the Young modulus on the normal direction and t the thickness of the cohesive zone.
The number of elements through the length of the cohesive zone should be enough to capture crack initiation and growth. The cohesive length is defined as the distance from the crack tip to the point where the maximum traction is attained and, based on mode I experimental testing, it can be computed as:

$$l_{cz} = ME\frac{G_C}{(t_{max})^2} \tag{4}$$

where M is a parameter depending on the loading condition and cohesive model (0 < M < 1), E is the Young modulus of the material, G_C is the fracture toughness and t_{max} is the maximum traction strength of the material.
Thus, the number of elements in the cohesive zone is $N_e = l_{cz}/l_e$, where l_e is the mesh size in the direction of the propagation of the delamination.

Cohesive Zone Modelling under Fatigue Load

Several considerations must be taken into account to implement fatigue into cohesive zone models, such as the load modelling, the damage accumulation by cycle, and the cycle jump strategy.
In general, authors separate the cyclic loading into two main categories: loading-unloading hysteresis damage model and envelope load damage model. Both are visually described in Figure 2 [12].
The loading-unloading hysteresis damage model is characterized takes into account the whole cyclic variation of the load, meaning that the maximum/minimum load and frequency characteristics are fully captured. This model is known to be computationally expensive and also known to be frequency-dependent. For its application in fatigue, a link between the critical stress and frequency must be established, as shown by Salih et al. [13].
On the other hand, in the envelope load model only the maximum load in the fatigue cycle is modelled and the variation is just taken into account by means of the load ratio. The load is therefore modeled as a continuous time-dependent variable, simplifying how the damage accumulation occurs cycle by cycle [12]. This model is the most used with cohesive elements since it allows to reduce the computational time and complexity.

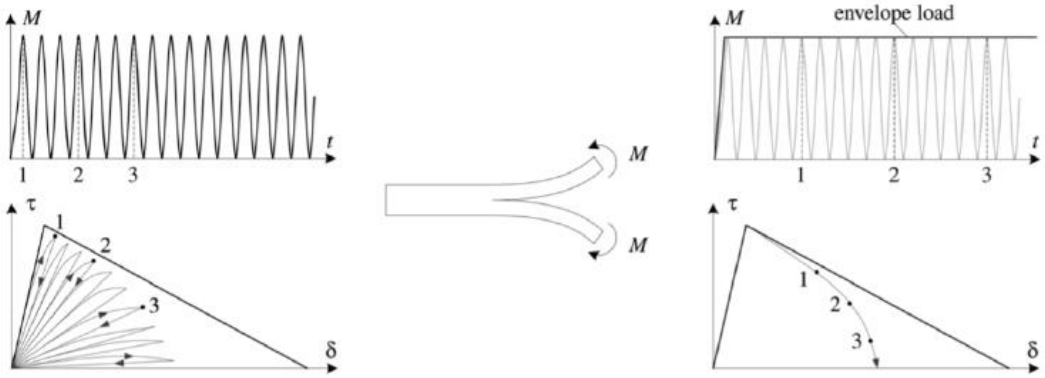

Figure 2 Loading-unloading hysteresis model (left) and envelope load damage model (right).

To evaluate the damage accumulation under fatigue loads, the damage is split into quasi-static and fatigue contributions, since the mechanisms of damage are different, and the overall damage is to be considered. Its expression is:

$$D_{total} = D_{static} + D_{fatigue} \tag{5}$$

The fatigue damage depends on the fatigue damage rate $\partial D/\partial N$. Turon [11] proposed a model dependent on the cohesive length, Paris' law and mixed-mode final and onset parameters, as in eqn. 6.

$$\frac{\partial D}{\partial N} = \frac{1}{A_{CZ}}\frac{\left(\delta^f(1-D) + D\cdot\delta^0\right)^2}{\delta^f\delta^0}\frac{\partial A}{\partial N} \tag{6}$$

where A_{CZ} is the the cohesive length by the out-of-plane thickness and $\partial A/\partial N$ is the crack growth rate (Paris' Law).

METHODS

Double Cantilever Beam

To analyse pure mode I, a double cantilever beam (DCB) specimen was selected. The results from the developed user-defined subroutine have been compared with the solution of built-in solver from Abaqus and experimental results available from Zavatta [4].

Two loading conditions were considered: quasi-static and fatigue loading. Abaqus does not have a built-in solver for fatigue condition, thus only the user-defined subroutine simulation was performed in this case.

The specimen geometry is shown in Figure 3. The aluminium adherends are modelled by solid elements, while the adhesive is modelled as a cohesive layer. For simplicity, a 2D numerical model is used.

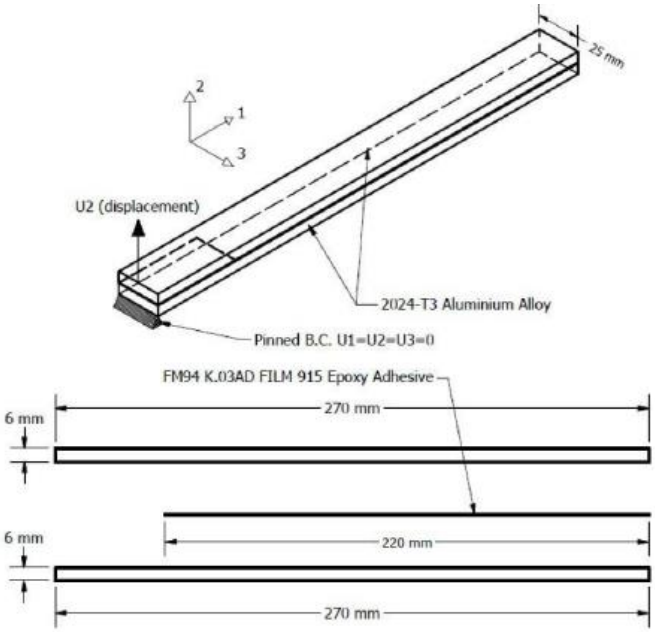

Figure 3: DCB dimensions, assembly and boundary conditions [4]

The adhesive material is a FM94K film, whose mechanical properties are described in table 1.

Table 1. Cohesive properties of adhesive layer FM94K [4].

Properties	*Symbol*		*Units*
Young's modulus	E	3000	MPa
Shear modulus	G	823	MPa
Poisson's ratio	υ	0.35	
Normal stiffness	K_n	$5\ 10^5$	N/mm^3
Tangent stiffness	K_t	$1\ 10^5$	N/mm^3
Cohesive strength (mode I)	t_1^0	50	MPa
Cohesive strength (mode II)	t_2^0	30	MPa
Fracture toughness (mode I)	G_{Ic}	1.70	N/mm
Fracture toughness (mode II)	G_{IIc}	3.06	N/mm

The mesh size in the cohesive zone was of 0.25 mm, so to have enough elements in the cohesive length, according to Turon [14]. For the fatigue case it was reduced for accuracy reasons to 0.10 mm.

For the quasi-static loading condition, two load steps are considered: the initial default step and the load step, where the displacement is applied. The fatigue case consists of three steps: the initial, the quasi-static load and the fatigue load. In this case, the quasi-static step can be considered as a crack initiation load, being the crack length computed at the end of this step the initial length for the fatigue load step.

The characteristics of the latter are specified in a way that the time period is equivalent to the number of cycles, and thus the increment sizes refer to the cycle size.
The load is applied through a fixed displacement set to 20 mm in the normal direction for the quasi-static case. For the fatigue case, an envelope loading approach was considered; various R-ratios were considered, as discussed later.
An UMAT subroutine was developed to simulate the cohesive element behaviour. The critical separation and the final separation are defined as:

$$\delta_3^0 = \frac{t_1^0}{K_n} \qquad ; \qquad \delta_3^f = \frac{2G_{Ic}}{K_n \delta_3^0} \tag{7}$$

At each time step t, the damage threshold, i.e. the point at which damage starts to accumulate, is computed as follows:

$$r^t = \frac{\delta_3^0 \delta_3^f}{\delta_3^f - D^t(\delta_3^f - \delta_3^0)} \tag{8}$$

Note that this value differs from the critical separation, in that its value depends on the current damage state and is updated at each time step.
If the current displacement jump is greater than the damage threshold defined in equation 8, the damage parameter is updated according to:

$$D^{t+1} = \frac{\delta_3^f (r^{t+1} - \delta_3^0)}{r^{t+1}(\delta_3^f - \delta_3^0)} \tag{9}$$

The stiffness matrix for pure mode I becomes:

$$K_{ij} = \begin{cases} \begin{bmatrix} K_n(1 - D^{t+1}) & 0 \\ 0 & K_t(1 - D^{t+1}) \end{bmatrix} & if\ \delta_3 \geq 0 \\ \begin{bmatrix} K_n & 0 \\ 0 & K_t(1 - D^{t+1}) \end{bmatrix} & if\ \delta_3 < 0 \end{cases} \tag{10}$$

If δ_3 is negative, the stiffness of the material is not affected (no damage accumulated).
Finally, the stresses can be evaluated by:

$$\sigma^{i+1} = K_{ij}\delta_j \tag{11}$$

For the fatigue load, the procedure is the same as the quasi-static loading condition. However, the contribution of fatigue to damage accumulation is calculated before the definition of the stiffness matrix. The theoretical constitutive model is based on Turon's work [11].
The total damage is the sum of the quasi-static and fatigue contribution:

$$D^{i+\Delta N} = D_{static}^{t+1} + D_{fatigue}^{i+\Delta N} \tag{12}$$

where the fatigue contribution of the current increment (i + ΔN) is based on the calculation of the parameters calculated on the previous increment (i):

$$D_{fatigue}^{i+\Delta N} = \frac{\partial D^i}{\partial N} \Delta N^i \tag{13}$$

The evolution of the damage variable $\partial D / \partial N$ is related to the crack growth rate, thus linking damage mechanics and fracture mechanics:

$$\frac{\partial D}{\partial N} = \frac{\partial D}{\partial A}\frac{\partial A}{\partial N} \tag{14}$$

The crack growth rate is defined by the Paris' law, in this specific case defined as:

$$\frac{\partial A}{\partial N} = \begin{cases} C\left(\frac{\Delta G}{G_{Ic}}\right) & if\ G_{th} < G^{max} < G_C \\ 0 & otherwise \end{cases} \tag{15}$$

The strain energy release rate G is computed as the area under the traction-separation law, as shown in Figure 4.

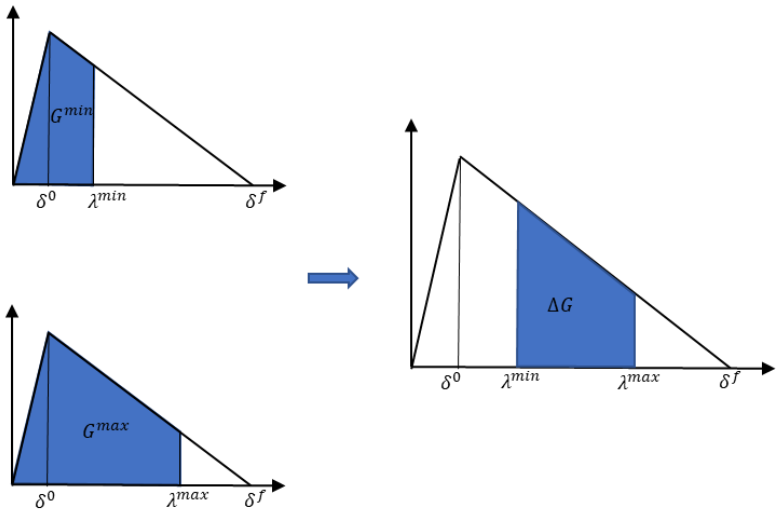

Figure 4: Strain Energy Release Rate (Maximum, Minimum and Variation) based on the Bi-Linear Traction Separation Law.

Finally, $\partial D/\partial A$ represents a material property relating damage and the damaged area and it is defined by the following equation:

$$\frac{\partial D}{\partial A} = \frac{1}{A_{cz}}\frac{(\delta_3^f(1 - D^{i+\Delta N}) + D^{i+\Delta N}\delta_3^0)^2}{\delta_3^f \delta_3^0} \tag{16}$$

where the cohesive area $A_{cz} = B \cdot l_{cz}$, being B the out-of-plane thickness and l_{cz} the length of the cohesive zone.

Cracked Lap Shear

To analyse mixed-mode loading, a Cracked Lap Shear (CLS) specimen was selected. In this case, only the fatigue case was computed via the user-defined subroutine simulation.

The specimen configuration, shown in Figure 5, was based on the work by van Teeseling [15] and Zavatta [4] on the study of the effect of Bolted Disbond Arrest Features (DAF) in a CLS specimen under fatigue loading.

Similarly to the DCB specimen, the FM94K adhesive layer is modelled as a cohesive layer, while the adherends are made of GLARE 2A-4/3-0.4 with Aluminum 2024-T3 plies and UD S2 FM94 GF prepreg plies. Again, a simplified 2D model was considered to reduce the computational complexity. The mesh size in the cohesive zone was 0.05 mm.

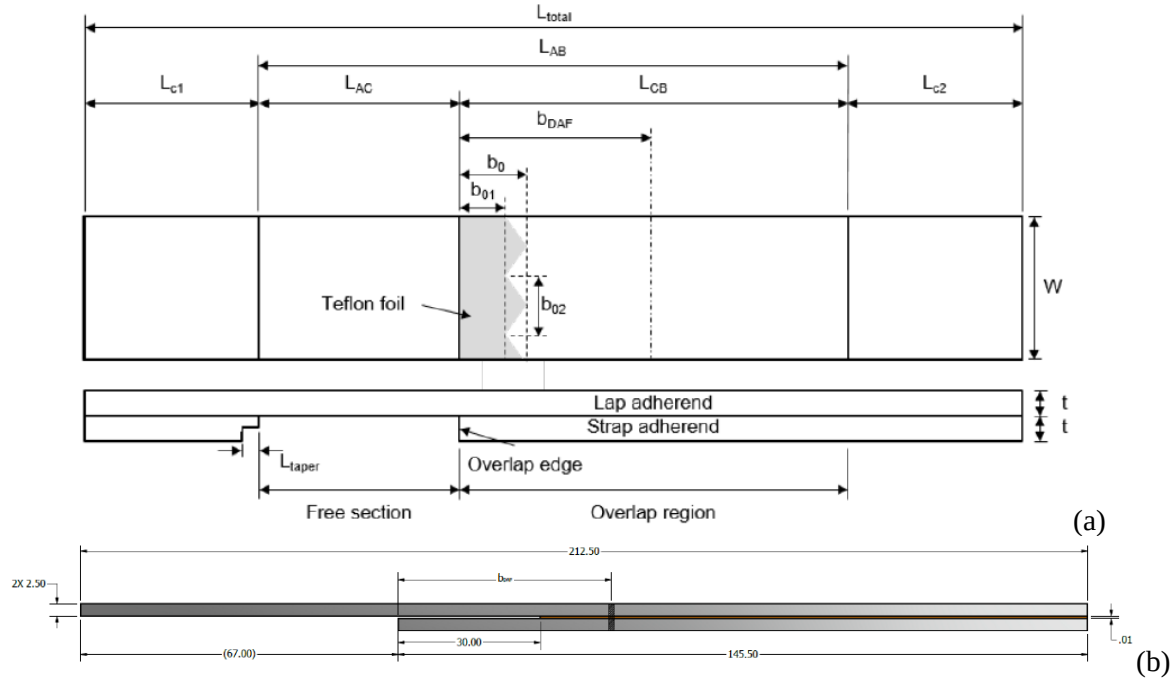

Figure 5: CLS testing specimen geometry (a) and numerical model (b).

Like in the DCB test, the fatigue case consists of three steps: the initial, the quasi-static load and the fatigue load. In this case, the quasi-static step can be considered as a crack initiation load, being the crack length computed at the end of this step the initial length for the fatigue load step. In the case a Disbond Arrest Feature is present, a step shall be added before the application of the quasi-static load, so to apply a clamping force to the bolt.
Boundary conditions and load positions are generally described for the finite element analysis in [15] and shown in figure 6.

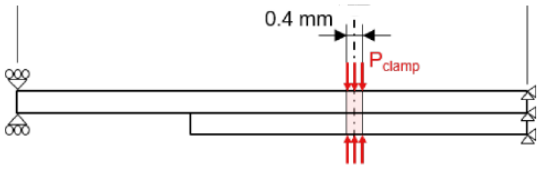

Figure 6: CLS boundary conditions and load positions.

The test has been performed under load-controlled conditions and, for the quasi-static step, it has been set to 26 kN and applied as a distributed pressure along the left edge of the top GLARE plate. For the fatigue step, an envelope loading with a constant R-ratio R=0.1 was considered.
Specimens with and without the Disbond Arrest Feature (DAF) have been considered. The bolt is modelled with a clamping pressure of 10 MPa as shown in the figure 6.
The UMAT subroutine was similar to the one illustrated for the DCB, with some notable differences to take into account the mixed-mode behaviour. For the definition of the damage criterion parameters, the local mix-mode ratio is defined [16]:

$$\beta = \frac{K_t \delta_{shear}^2}{K_t \delta_{shear}^2 + K_n \langle \delta_3 \rangle^2} \tag{17}$$

Which allows the definition of the mode-dependent penalty stiffness:

$$K_\beta = K_n(1-\beta) + \beta K_t \tag{18}$$

The mixed-mode critical displacement is defined by means of the Benzeggagh-Kenane delamination propagation law (B-K Law) [17] as:

$$\delta^0 = \sqrt{\frac{K_n(\delta_3^0)^2 + [K_t(\delta_{shear}^0)^2 - K_n(\delta_3^0)^2]\beta^\eta}{K_\beta}} \tag{19}$$

with exponent η=1.75 [18].
The evolution of the damage variable $\partial D/\partial N$ is again related to the crack growth rate as in eqn. 14. However, the crack growth rate is computed according to the model developed by Bürger [19] for mixed-mode loading:

$$\frac{\partial A}{\partial N} = \begin{cases} C\left(\Delta\sqrt{G_{1eq}}\right)^m & if\ \sqrt{G_{theq}} < \sqrt{G_{1eq}^{max}} < \sqrt{G_{Ceq}} \\ 0 & otherwise \end{cases} \tag{20}$$

Here, the equivalent mixed-mode strain energy release rate is defined as:

$$\sqrt{G_{1eq}} = \frac{\sqrt{G_I}}{2} + \sqrt{\frac{G_I}{4} + G_{II}} \tag{21}$$

This expression is used to calculate $\sqrt{G_{theq}}$, $\sqrt{G_{1eq}^{max}}$ and $\sqrt{G_{Ceq}}$.
Thus, the variation of the strain energy release rate is computed as:

$$\Delta\sqrt{G_{1eq}} = \left(\sqrt{G_{1eq}^{max}}(1 - R^2)\right)^2 \tag{22}$$

The coefficient C in eq. 20 is calculated according to:

$$C(\beta) = C_{100\%}^{\beta} C_{0\%}^{1-\beta} \tag{23}$$

where the coefficients for FM94K [15, 19] are reported in the following table:

Table 2. Coefficients of Bürger's model for FM94K

$C_{0\%}$	$C_{100\%}$	$m_{0\%}$
5.27 10^{-17}	2.07 10^{-18}	3.78

Finally, $\partial D/\partial A$ is defined as in eqn. 18.

RESULTS

Double Cantilever Beam (DCB) - Quasi-Static Load

The effectiveness of the Abaqus numerical model through material user-defined subroutines, UMAT, has been compared with experimental results from Zavatta [4] on the disbonding behaviour in a double cantilever beam (DCB) specimen.

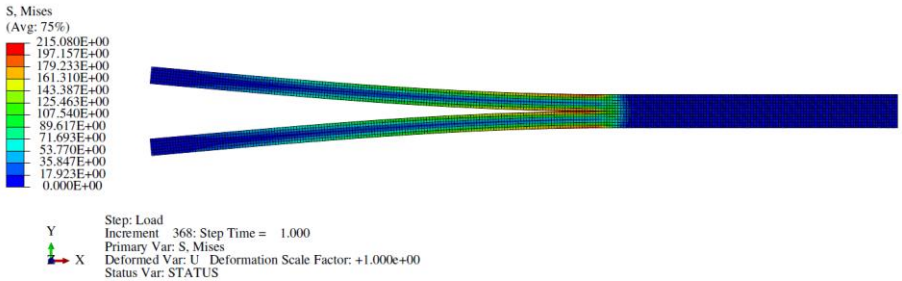

Figure 7: Visual representation of the von-Mises Stresses (S) results for the UMAT with quasi-static loading [scale in MPa].

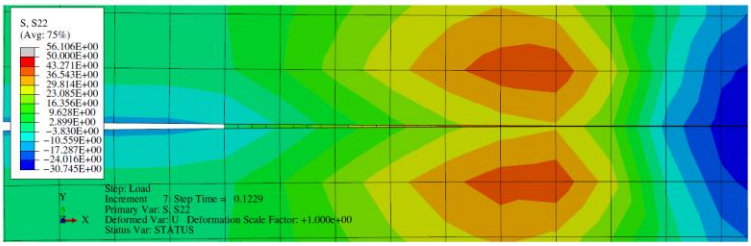

Figure 8: Detail of normal stresses in the adhesive before crack growth under quasi-static loading [scale in MPa].

In figure 7, the distribution of the von Mises stresses along the tested specimen at the end of the load step is shown. The stress concentration around the tip is related to the resistance of the adhesive to crack.
The normal stress component at the crack tip before the initiation of the crack growth (failure of the cohesive elements) is shown in figure 8. Those stresses in the adhesive layer do not exceed 50 MPa, the cohesive maximum strength. The stress behaviour follows the bi-linear traction separation law: after reaching the maximum strength, the strength in the cohesive elements decreases because of the local damage.

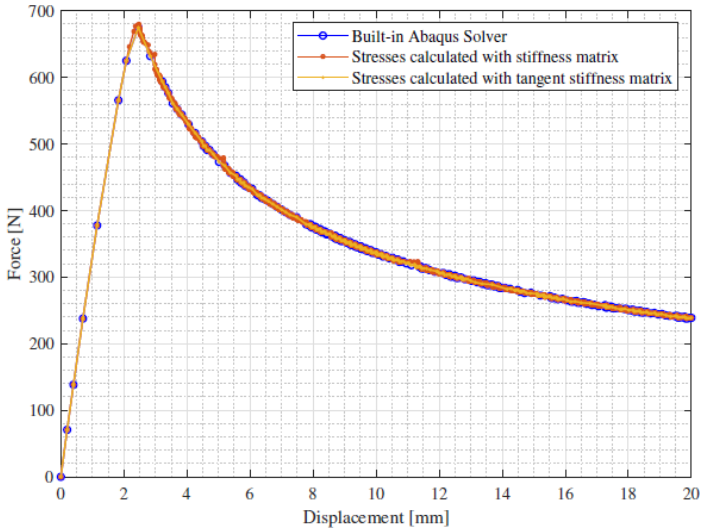

Figure 9: Load - Displacement of DCB specimen with different stress definitions on the UMAT and comparison with the Abaqus Built-in Solver under quasi-static loading.

The simulations with the UMAT were performed with two different stress definitions, as described in the methods section, by means of the stiffness matrix (Eqn. 13) method. The results in terms of force/displacement were compared with the solution obtained using Abaqus built-in Cohesive Elements (see Figure 9), showing good agreement. Those results have been checked by Zavatta [4] by comparison with experimental tests.

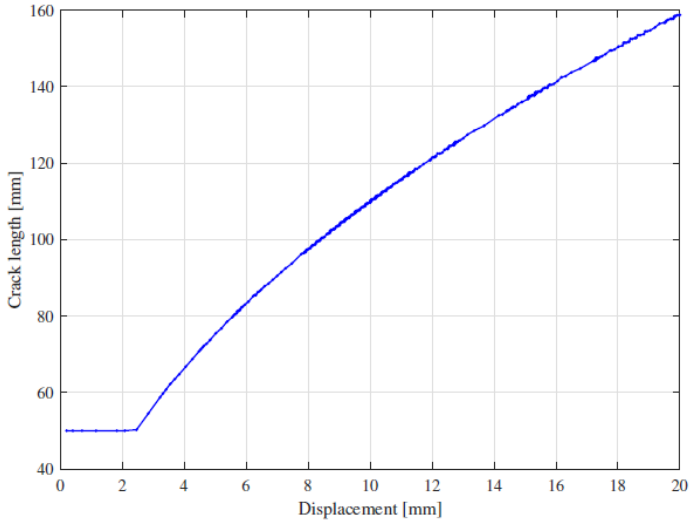

Figure 10: Crack Length-Displacement of DCB specimen with the UMAT under quasi-static loading.

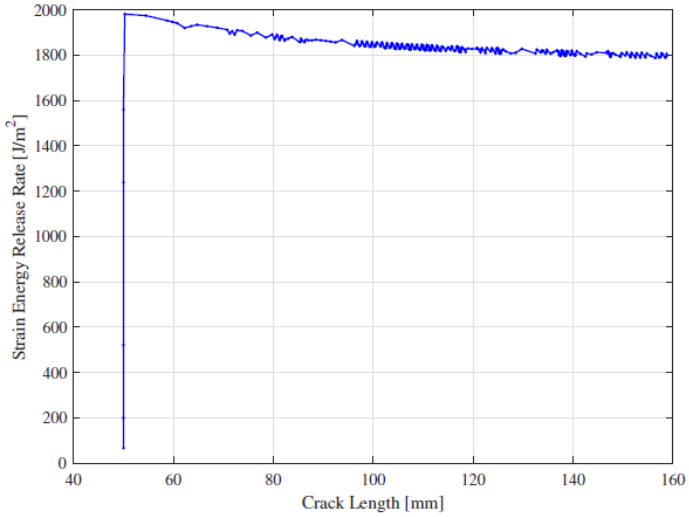

Figure 11. Numerical evaluation through UMAT of the Strain Energy Release Rate (G_I) vs Crack Length for DCB specimen under quasi-static loading.

The crack length vs. displacement graph is shown in Figure 10. The crack starts growing after the cohesive strength is reached. Finally, the strain energy release rate was calculated by means of the modified beam theory (eqn. 37) and plotted against the crack length, as shown in figure 11. The asymptotic value of the SERR, 1800 J/m^2, which is the critical energy release rate used for the cohesive model, shows a good agreement with literature [4].

$$G_I = \frac{3Fd}{2ba} \tag{24}$$

where F is the applied load, d is the displacement, b is the out-of-plane thickness of the specimen, and a is the crack length.

Double Cantilever Beam (DCB) - Fatigue Load

The results from 2D numerical analysis for the DCB specimens under fatigue loading condition were compared with experimental data by Pascoe [20]. Six specimens were tested, and the post-processed data was further analysed to obtain the modified Paris' law coefficients (equation 15). The coefficients were calculated by the curve fitting tool in MATLAB and summarized in table 3.

Table 3. Modified Paris' Law Parameters.

Specimen	*Load-Ratio (R)*	*C*	*m*	*Displacement [mm]*
G-002-II	0.29	1.4775	6.3322	5.083
G-010-II	0.036	0.58133	4.9545	2.893
H-002-II	0.036	0.4185	5.1144	6.27
H-003-II	0.29	2.4102	6.8236	5.13
H-004-I	0.61	30.9195	9.3777	2.3275

Fatigue 2D simulations via the UMAT subroutine of the specimens were performed successfully under the conditions described previously. In figure 12, the stress distribution of the specimen is shown at the start and at the end of the fatigue step (1 10^6 cycles).

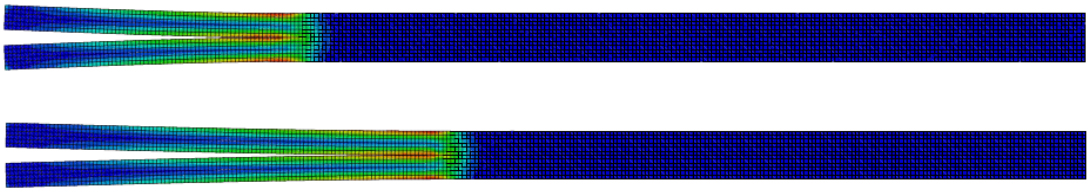

Figure 12. Visual comparison of crack length at the beginning (a) and end (b) of the fatigue step with UMAT subroutine for the G-002-II specimen.

For every specimen, the crack growth rate vs the strain energy release ratio and the crack length vs the number of fatigue cycles were plotted, comparing the data obtained by the 2D simulations through UMAT, and the experimental data by Pascoe [3]. As an example, the results for the G-010-II specimen are shown in Figure 13. Similar results have been obtained for the other configurations.

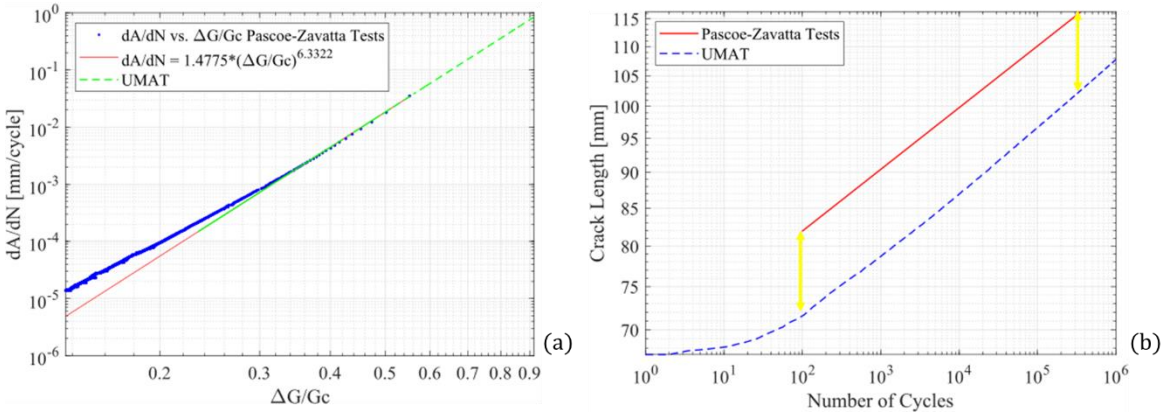

Figure 13. Comparison between simulation and experimental results for the G-002-II specimen: (a) Crack growth rate vs Strain energy release rate ratio, (b) Crack length vs load cycles.

In the case of the crack growth rate plots, the simulation results are in good agreement with the fit function of the experimental data. On the other hand, a difference between numerical and experimental results can be underlined in the crack length plots. In particular, the initial crack length computed by the numerical model is higher than that measured experimentally, which results in the plot of the computed crack length being shifted upwards. The explanation of this behaviour is related to the pre-cracking procedure during experimental testing, where the specimen was loaded before the start of fatigue crack growth to remove the effect of the resin-rich area at the tip of the delamination. The crack growth rate in the simulation is based on the fitting coefficients from experimental tests, evaluated in MATLAB. All the fittings had a $R^2 > 0.90$, indicating a high correlation between the fitting function and the experimental data. Despite the differences of the initial crack length in the fatigue cycle, the

experimental and simulation curves are almost parallel, which indicate a similar behaviour under fatigue conditions.

Cracked Lap Shear (CLS)

As discussed in the Methods section, the analysis of a cracked lap shear (CLS) configuration with and without a bolted Disbond Arrest Features (DAF) was performed by means of a material user-defined subroutine. The numerical results were compared with the experimental data in [1].

2D Simulations were performed under fatigue loading (which includes a quasi-static step). The load-displacement curve for the quasi-static load is shown in Figure 18.

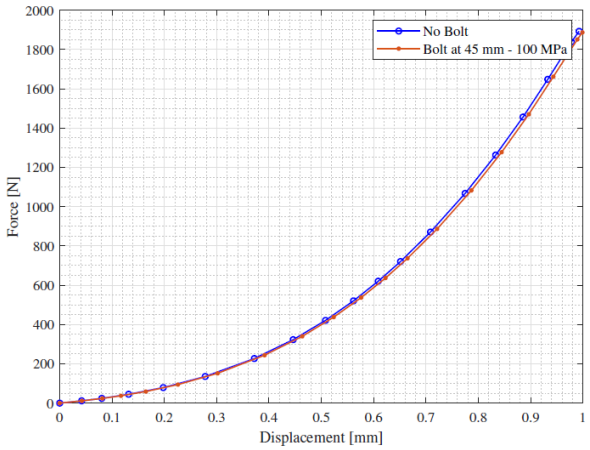

Figure 18. Load-Displacement of CLS specimen with and without DAF under quasi-static loading.

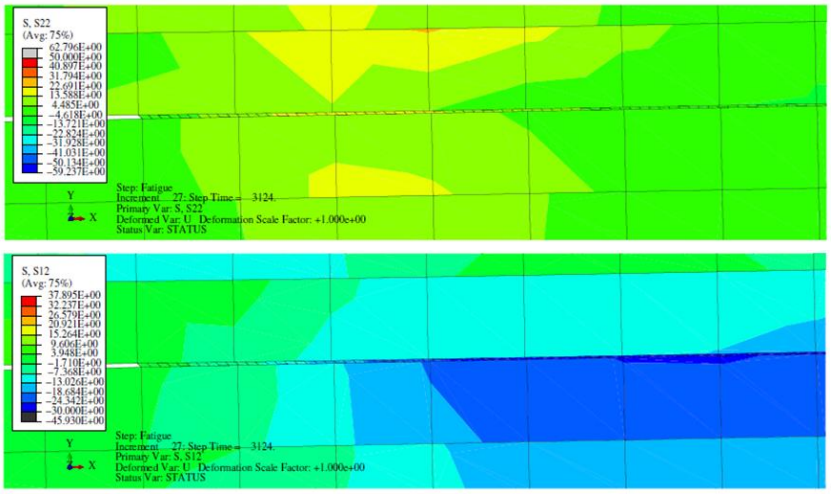

(a)

(b)

Figure 19: Stress distribution [MPa] around the crack tip before crack growth for CLS specimen with DAF: a) S22 direct stress, b) S12 shear stress.

The normal (a) and shear (b) stresses around the crack tip during the fatigue step, before the initiation of crack growth (failure of the cohesive elements), are shown in figure 19. As expected, the maximum cohesive strength of 50 MPa for the normal direction and 30 MPa for the shear direction are not exceeded.

The 2D simulations under fatigue load were performed with and without DAF. As shown in figure 20, before the quasi-static load step the DAF is pre-loaded, with a resulting stress distribution as in (a). At the end of the following steps (quasi-static and fatigue), the von Mises stress distribution shows higher values around the crack tip, following the crack propagation.

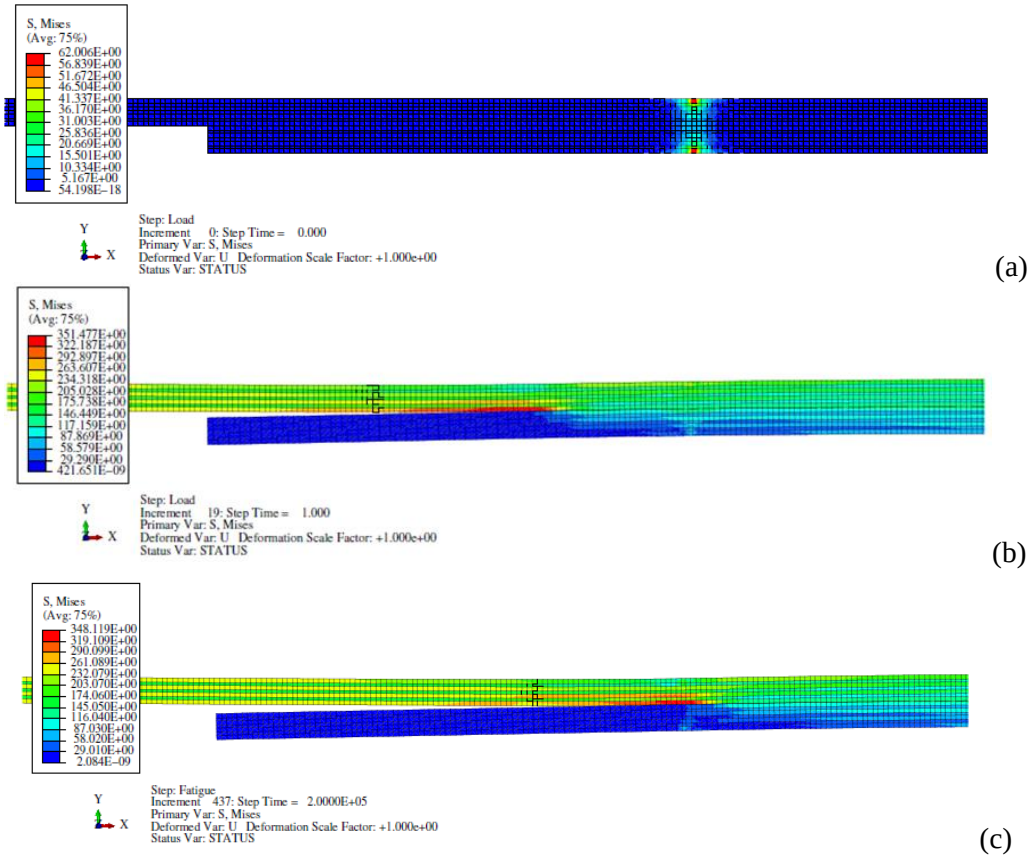

Figure 20: von Mises stress distribution at the end of each step: a) Bolt Pre-Load, b) Quasi-static and c) Fatigue for CLS specimen with DAF.

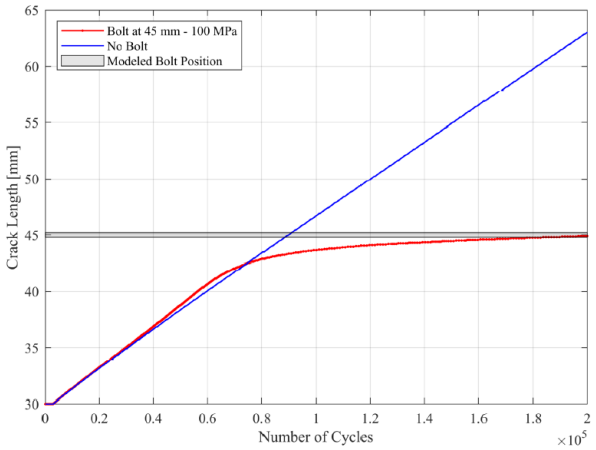

Figure 21: Crack length - number of fatigue cycles in CLS specimen with and without DAF under fatigue loading.

Figure 21 shows the increase of crack length with respect to the number of cycles. For the case with no DAF, the crack keeps growing at a constant rate as expected. The same constant crack growth can also be seen in Figures 22 and 23, showing the crack growth rate as function respectively of the crack length and the number of cycles.

In the case of the presence of the bolt as DAF, the crack growth slows down as the crack tip gets closer to the position of the bolt, which can be seen by the change of slope of the curve. The reduction of the crack growth rate is shown in Figures 22 and 23.

The results for both the cases with and without DAF are in accordance with the results shown by van Teeseling [1] for the 2D geometry, thus validating the UMAT subroutine developed for this paper in the mixed-mode loading conditions.

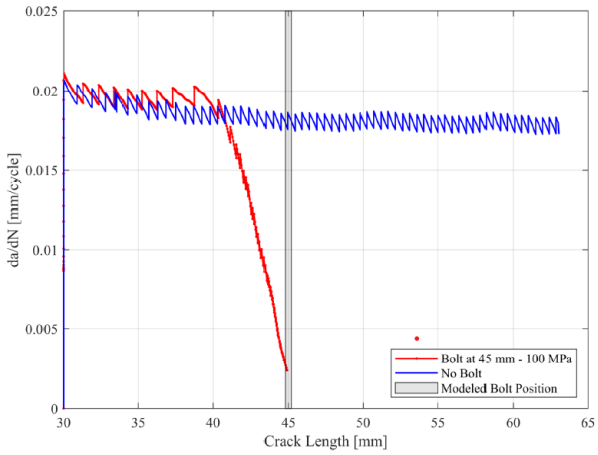

Figure 22: Crack growth rate - crack length in CLS specimen with and without DAF under fatigue loading.

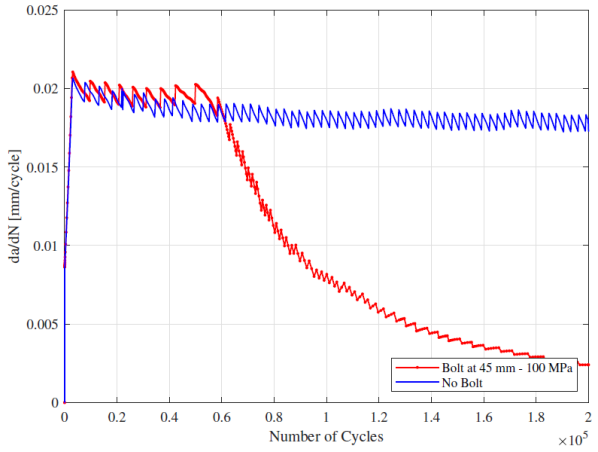

Figure 23: Crack growth rate - number of fatigue cycles in CLS specimen with and without DAF under fatigue loading.

On the other hand, the numerical results for the 2D geometry cannot take into account the full 3D distribution of stresses, as shown by Zavatta [5]. Indeed, in a 3D case, the DAF does not cover the whole width of the specimen as in the 2D simulations. This clearly affects the overall crack growth, that in the 2D case is completely arrested by the DAF. In fact, in the tested specimens some growth in the width direction can be measured even past the position of the bolt.

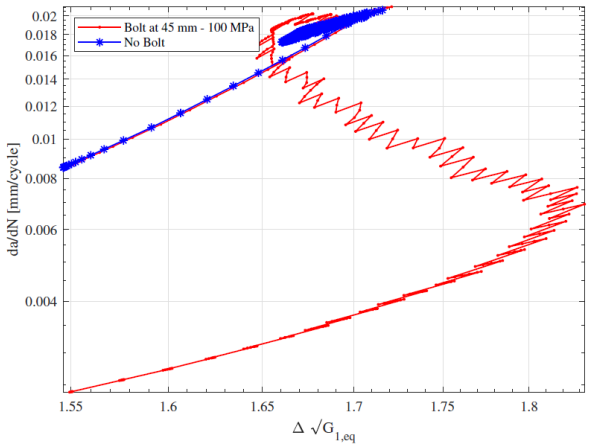

Figure 24: Crack growth rate - Variation of the Equivalent Energy Release Rate in CLS specimens with and without DAF under fatigue loading.

The simulations show that the DAF is effective in suppressing the opening mode, thus reducing the crack growth rate. Figure 24 shows the modified Paris' Law with the equivalent SERR from Bürger's model. The model with no bolt shows a linear behaviour as expected, while the effect of the DAF results in a non-linear behaviour. This effect may be explained with the help of figure 25, where the mixed-mode ratio is plotted against the position along the adhesive layer at the end of the fatigue step. In the case with the DAF, when the crack is approaching the bolt position the mode I opening is reduced due to the pressure of the DAF. Conversely, without the DAF the mixed mode opening is always dominant. This change of mixed-mode ratio as the crack front comes closer to the bolt position affects the crack growth rate, since the Paris' law coefficients depend on the mixed-mode ratio. Overall, for both the cases with and without DAF, the damage is accumulated mostly by mode II loading, due to the applied shear loading in CLS specimens.

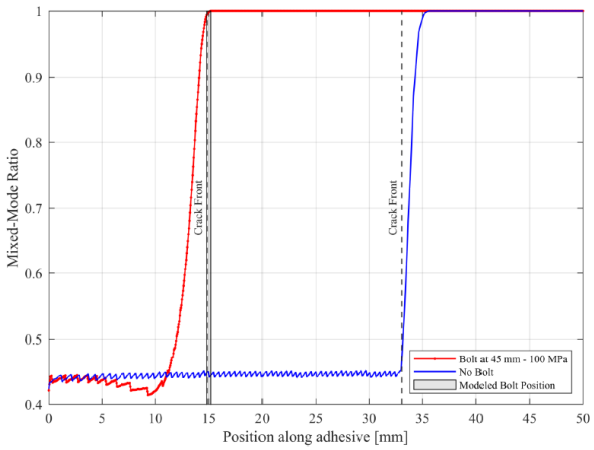

Figure 25: Mixed-Mode ratio (β) - position along the adhesive in CLS specimens with and without DAF at the end of the fatigue load step.

CONCLUSIONS

In this work, Abaqus numerical simulations of crack growth in adhesively bonded joints under quasi-static and fatigue loading conditions were performed for different specimen geometries.
User-defined subroutines were developed to perform simulations under quasi-static and fatigue loading in 2D models. The Material User-defined Subroutines (UMAT) were used to implement the cohesive zone models, allowing the simulation of crack growth in the joints.
A Double Cantilever Beam (DCB) specimen was analysed under pure mode I opening. The pure mode I allowed the implementation of a simpler cohesive model in the UMAT for both quasi-static and fatigue loading cases. The quasi-static loading case was validated by comparing the results with both experimental and Abaqus built-in solver data. The fatigue loading case was validated by comparing the numerical results with experimental results, since the built-in solver cannot handle fatigue loading. The results show the same crack growth behaviour between simulated and experimental measured data, while the initial crack length was different, since experimental specimens were pre-cracked at the beginning of the crack growth phase.
For mixed-mode opening, a Cracked Lap Shear (CLS) specimen was simulated. Implementing the mixed mode allowed the simulation of more realistic loading conditions. The mixed-mode user-defined subroutine was validated with experimental results, taking into account the effect of a Disbond Arrest Feature (DAF). In the specimen without DAF, the crack opening is always under mixed-mode conditions (due shear and tension loading), and calculated crack growth followed the Paris' Law. On the other hand, in the presence of the DAF, the mode I opening was suppressed, resulting in a reduction of crack growth and a change of the mixed-mode ratio as the crack front approached the bolt. Further studies on the behaviour of the crack front in presence of a disbond arrest feature shall be performed, since only 2D results are presented in this paper and the 3D behaviour observed in experimental tests

shows additional features. Thus, it is recommended to develop a user-defined subroutine based on the present work for the 3D case.

REFERENCES

[1] Mazumdar, S. (2001). *Composites Manufacturing: Materials, Product, and Process Engineering*. CRC Press, Boca Raton.

[2] Hart-Smith, L. J. (2005). In: *Adhesive Bonding, Woodhead Publishing Series in Welding and Other Joining Technologies*, pages 489–527. Adams, R. D. (Ed.), Woodhead Publishing.

[3] Pascoe, J.A. (2016). *Characterisation of Fatigue Crack Growth in Adhesive Bonds*. PhD thesis, TU Delft, Delft.

[4] Zavatta, N. (2020). *Crack growth in adhesively bonded joints under quasi-static and fatigue loading*. PhD Thesis, Alma Mater Studiorum - Università di Bologna, Bologna.

[5] Zavatta, N., and Troiani, E., (2020). *Lecture Notes in Mech. Eng.*, Proceedings of the 30th ICAF Symposium, vol I, pp. 360–371

[6] Wisnom, M.R. (2012). *Philos T Roy Soc A*, vol. 370(1965), pp 1850–1870.

[7] De Moura, M.F. (2008). In: *Delamination Behaviour of Composites, Woodhead Publishing Series in Composites Science and Engineering*, pages 310-326. Sridharan, S. (Ed.), Woodhead Publishing.

[8] Löbel, T., Sonnenberg, H., Holzhüter, D., and Hühne, C. (2015). In: *10th International Conference on Composite Science and Technology*, Araúo, A.L. et al. (Ed.) Lisbon, Portugal.

[9] Park K., and Paulino G.H. (2011). *App. Mech. Rev*., vol. 64 (6), pp 1002-1021

[10] Camanho, P.P., Turon, A., and Costa, J. (2008). In: *Delamination Behaviour of Composites, Woodhead Publishing Series in Composites Science and Engineering*, pages 485–513. Sridharan, S. (Ed.), Woodhead Publishing.

[11] Turon A., (2007). *Simulation of delamination in composites under quasistatic and fatigue loading using cohesive zone models*. PhD thesis, Universitat de Girona, Girona.

[12] Bak, B., Sarrado, C., Turon, A., and Costa, J. (2014). *App. Mech. Rev*., 66 (6)

[13] Salih, S., Davey, K., and Zou, Z. (2018). *Int. J. Solids Struc.*, vol 152-153, pp 228–237.

[14] Turon, A., Dávila, C.G., Camanho, P.P., and Costa, J. (2007). *Eng. Fract. Mech*, vol. 74(10), pp 1665–1682,

[15] Van Teeseling, I. (2019). *Towards the Certification of Bonded Primary Fiber Metal Laminate Structures by Bolted Disbond Arrest Features*. PhD Thesis, TU Delft, Delft.

[16] Turon, A., González, E.V., Sarrado, C., Guillamet, G., and Maimí, P. (2018). *Composite Structures*, vol 184, pp: 506–511.

[17] Benzeggagh, M.L., and Kenane, M. (1996). *Compos. Sci. Technol.*, vol 56(4), pp: 439–449.

[18] Naik, S.H., and Javagal, S. (2019). *Procedia Structural Integrity*, vol. 14, pp 900–906.

[19] Bürger, D.B. (2015). *Mixed-Mode Fatigue Disbond on Metallic Bonded Joints.* PhD thesis, TU Delft, Delft.

[20] Pascoe, J.A., Zavatta, N., Troiani, E. and Alderliesten, R.C. (2020). *Eng. Fract. Mech.*, vol. 229, 106959.

[21] Knoop, H. (2016). *Numerical Simulation of failure of adhesively bonded composite parts using the cohesive zone method*. Thesis, Hochschule für angewandte Wissenschaften Hamburg.